ACS OMEGA

Open Access

http://pubs.acs.org/journal/acsodf

Article

Insight into the Photocatalytic Degradation Mechanism for "Forever Chemicals" PFNA by Reduced Graphene Oxide/WO_3 Nanoflower Heterostructures

Kaelin Gates, Shivangee Rai, Avijit Pramanik, Olorunsola Praise Kolawole, Sanchita Kundu, Mine Ucak-Astarlioglu, Manoj K. Shukla, Ahmed Al-Ostaz, and Paresh Chandra Ray*

Cite This: *ACS Omega* 2025, 10, 10675−10684

Read Online

ACCESS | Metrics & More | Article Recommendations | Supporting Information

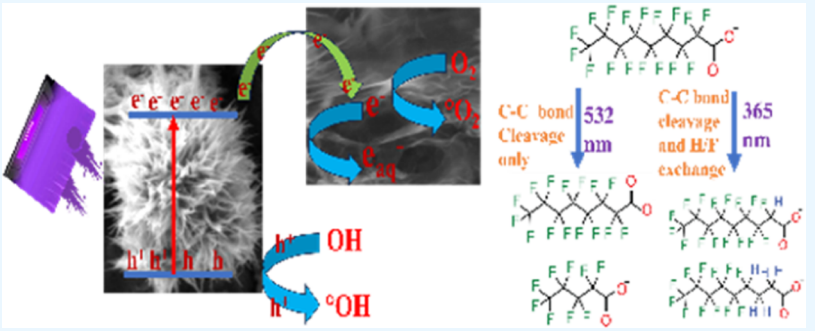

ABSTRACT: Water contamination with "forever chemicals" like per- and polyfluoroalkyl substances (PFAS) poses significant toxicity to the environment. Since they are the most persistent synthetic chemicals that hardly degrade in the natural environment and are carcinogenic to humans, there is an urgent need to discover novel processes for destroying PFAS. Herein, we report on the design of a reduced graphene oxide (r-GO)/WO_3 nanoflower (WO_3-NF)-based heterostructure for harnessing 365 nm light-driven photocatalytic oxidation and reduction process toward the photocatalytic degradation of perfluorononanoic acid (PFNA). Moreover, reported data reveal that using an r-GO/WO_3-NF heterostructure photocatalyst, 100% PFNA degradation and 14% defluorination can be achieved in the presence of isopropyl alcohol as the hydroxy radical ($^{\bullet}OH$) quencher or glucose as a hot hole (h^+) quencher after exposure to 365 nm light for 22 h. A reported mechanistic study shows synergistic oxidation and reduction processes are vital for the complete degradation of PFNA, where the hydrated electron (e_{aq}^-) plays a key role as a reducing agent and h^+ and $^{\bullet}OH$ act as oxidation agents. Furthermore, the photocatalytic destruction mechanism study indicates that chain shortening via C−C bond breaking and defluorination via C−F bond breaking are major pathways for PFNA degradation. A wavelength-dependent study shows that only 22% degradation can be achieved after exposure to 532 nm light for 22 h, which is due to the lack of the formation of hydrated electrons (e_{aq}^-). The current study sheds light on the construction of the r-GO/WO_3 NF heterojunction for the highly efficient degradation of PFAS.

1. INTRODUCTION

Per- and polyfluoroalkyl substances (PFAS) have been utilized for over 70 years in food packaging, automotive materials, fire-fighting foams, cosmetics, and cookware.[1−10] As per the U.S. Environmental Protection Agency (EPA), perfluorononanoic acid (PFNA) and perfluorooctanoic acid (PFOA) are often detected PFAS in the environmental samples in the range of 6.5 ppm (ppm) in groundwater, which is 5 orders of magnitude higher than the EPA health advisory level for the drinking water (0.070 ppb).[1−10]

As per the Centers for Disease Control and Prevention (CDC), PFAS are found in the blood serum routinely and have been linked with testicular, kidney, thyroid, and breast cancer.[2] Since PFAS contain multiple highly stable C−F bonds, whose bond dissociation energy is very high (117.8−123.4 kcal/mol),[7−20] PFAS exhibit more than 50 years of half-life in the human body and more than 500 years half-life in the environment.[1−10] Since those "forever chemicals" are resistant to degradation by conventional wastewater treatment in the environment or in the human body, there is an urgent need to discover novel technology that can destroy PFAS.[12−22] Driven by the need, in the current manuscript, we report the design of reduced graphene oxide (r-GO)-WO_3 nanoflower (WO_3 NF)-

Received: January 2, 2025
Revised: February 9, 2025
Accepted: February 13, 2025
Published: March 4, 2025

https://doi.org/10.1021/acsomega.5c00054
ACS Omega 2025, 10, 10675−10684

Scheme 1. (A) Scheme of the Possible Pathways of the Photocatalytic Degradation of Perfluorononanoic Acid (PFNA) Using the r-GO/WO_3 NF Heterostructure Catalyst

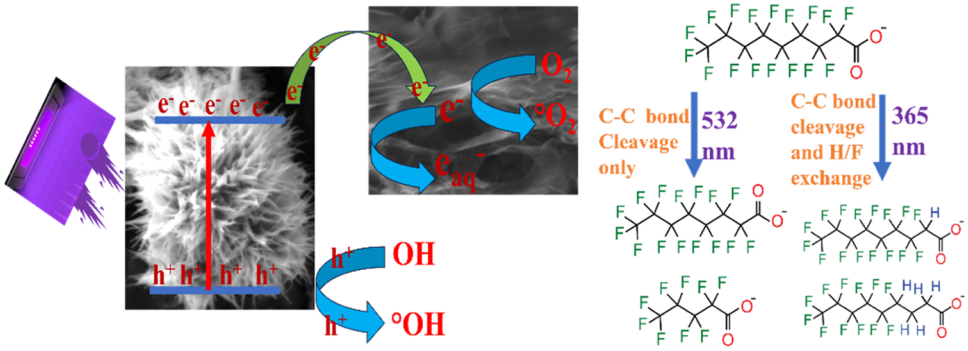

based binary heterojunction for harnessing the light-driven photocatalytic oxidation and reduction process for the photocatalytic degradation of (PFNA).

Since PFAS exhibits strong absorption below 250 nm, direct photodegradation using light above 300 nm is unrealistic.[10−22] Among all of the recently reported photodegradation technologies for PFAS, photocatalysis can be a promising technology for PFAS destruction, where the hydrated electron with extremely negative reduction potential (e_{aq}^-, $E_0 = -2.9$ V) has been used for the effective degradation of C−F bonds.[8−22] In the case of photocatalytic degradation using WO_3, TiO_2, and other semiconductor catalysts, upon irradiation of light, electrons are excited from the valence band (VB) to the conduction band (CB).[23−39] As a result, the above process generates hot holes (h^+) in the valence and hot electrons (e^-) in the conductance band.[20−36] Although hot holes (h^+) and hot electrons (e^-) can be used for the degradation of organic compounds due to the high recombination rate of photoinduced electron−hole pairs, the practical performance of WO_3, TiO_2, $W_{18}O_{49}$, and other semiconductor catalysts are dissatisfactory.[22−39] To overcome the above problem, as reported in Scheme 1, we have designed an r-GO/WO_3 NF-based binary heterojunction, where the Schottky heterojunction formed between r-GO and the WO_3 NF can effectively separate photogenerated carriers. Since the above process prevents the electron−hole pair recombination, it will allow enhancing the photocatalytic efficiency for the degradation of PFAS.[8−20] Moreover, r-GO with a large specific surface area has been used to improve charge carrier mobility, where reduced graphene oxide acts as an efficient acceptor and mediator for photoinduced electrons.[1−10] A fraction of these photoinduced electrons is released into the solvent and formed hydrated electrons (e_{aq}^-),[5−20] which are known to be the most reactive nucleophilic species and have been used as a reducing agent to cleave C−F bonds.[5−20] Also, during photodegradation, the binary r-GO/WO_3 NF heterostructure that has been used to produce oxidizing agents like hole (h^+) and hydroxyl radical ($^•OH$), which has a huge potential to degrade PFNA.[10−20] It is now well recognized that in the case of PFAS degradation, due to the strong shielding effect induced by the high electron cloud density around fluorine atoms, the defluorination percentage is significantly weak.[7−22] To improve the defluorination percentage, we used the r-GO/WO_3 NF heterostructure-based photocatalyst wherein simultaneous participation of reduction and oxidation processes can substantially enhance the overall defluorination rate.[8−20]

2. EXPERIMENTAL SECTION

2.1. Synthesis of Reduced Graphene Oxide (r-GO). Reduced graphene oxide (r-GO) was developed using two stem synthesis procedures.[23−26,35−37] For this purpose, in the first step, two-dimensional (2D) graphene oxide was synthesized from natural graphite powder using the modified Hummer method, as we and others have reported before.[23−26,35−37] Experimental details are reported in the Supporting Information. In the second step, for the development of reduced graphene oxide (r-GO), we have reduced freshly prepared graphene oxide using ascorbic acid as a reducing agent.[23−26,35−37] At the end, r-GO was characterized by using different microscopic and spectroscopic techniques.[24−27] Figure 1C shows the scanning electron microscopy (SEM) morphology for freshly prepared r-GO.[23−26,35−37] Inserted high-resolution transmission electron microscopy (HRTEM) images in Figure 1C show the lattice fringe spacing to be around 0.34 nm, which is due to the (002) plane of graphene oxide. Figure 1D shows the energy-dispersive X-ray (EDX) spectroscopy mapping,[23−26,35−37] which indicates the presence of C and O in reduced graphene oxide. Figure S1 in the Supporting Information shows the X-ray diffraction (XRD) spectra from r-GO, which shows the broad (002) planes at 25.8° for r-GO (JCPDS card number 05-0664).[23−26,35−37]

2.2. Synthesis of the WO_3 Nanoflower (NF). For the development of the WO_3 nanoflower heterostructure, we used the hydrothermal synthetic approach.[38,39] Experimental details have been reported in the Supporting Information. In brief, 0.6 g of sodium tungsten dehydrate ($Na_2WO_4·2H_2O$) was dissolved in 60 mL of deionized water while stirring at room temperature to form a transparent solution.[38,39] Then, 3 mL of HCl (37%) was added to form a yellowish precipitate of tungstic acid (H_2WO_4). Next, 0.30 g of oxalic acid ($C_2H_2O_4·2H_2O$) was added to the suspension at a high rate of stirring. After that, the mixture was introduced into a Teflon-lined stainless steel autoclave.[38,39] In the next step, a hydrothermal reaction was performed at 190 °C for 6 h. In the end, the green precipitates of nanoflowers were dried at 60 °C for 3 h. After that, the WO_3 nanoflower was characterized by using different microscopic and spectroscopic techniques.[24−27] Figure 1A shows the scanning electron microscopy (SEM) morphology for the freshly prepared WO_3 nanoflower, which indicates that the nanoflower has a diameter of 200 ± 50 nm.[23−26,35−37] Figure S2 in the Supporting Information shows the energy-dispersive X-ray (EDX) spectroscopy spectra,[23−26,35−37] which indicate the presence of W and O in WO_3 NF. Figure 1B shows the tunneling electron microscopy (TEM) morphology

https://doi.org/10.1021/acsomega.5c00054
ACS Omega 2025, 10, 10675−10684

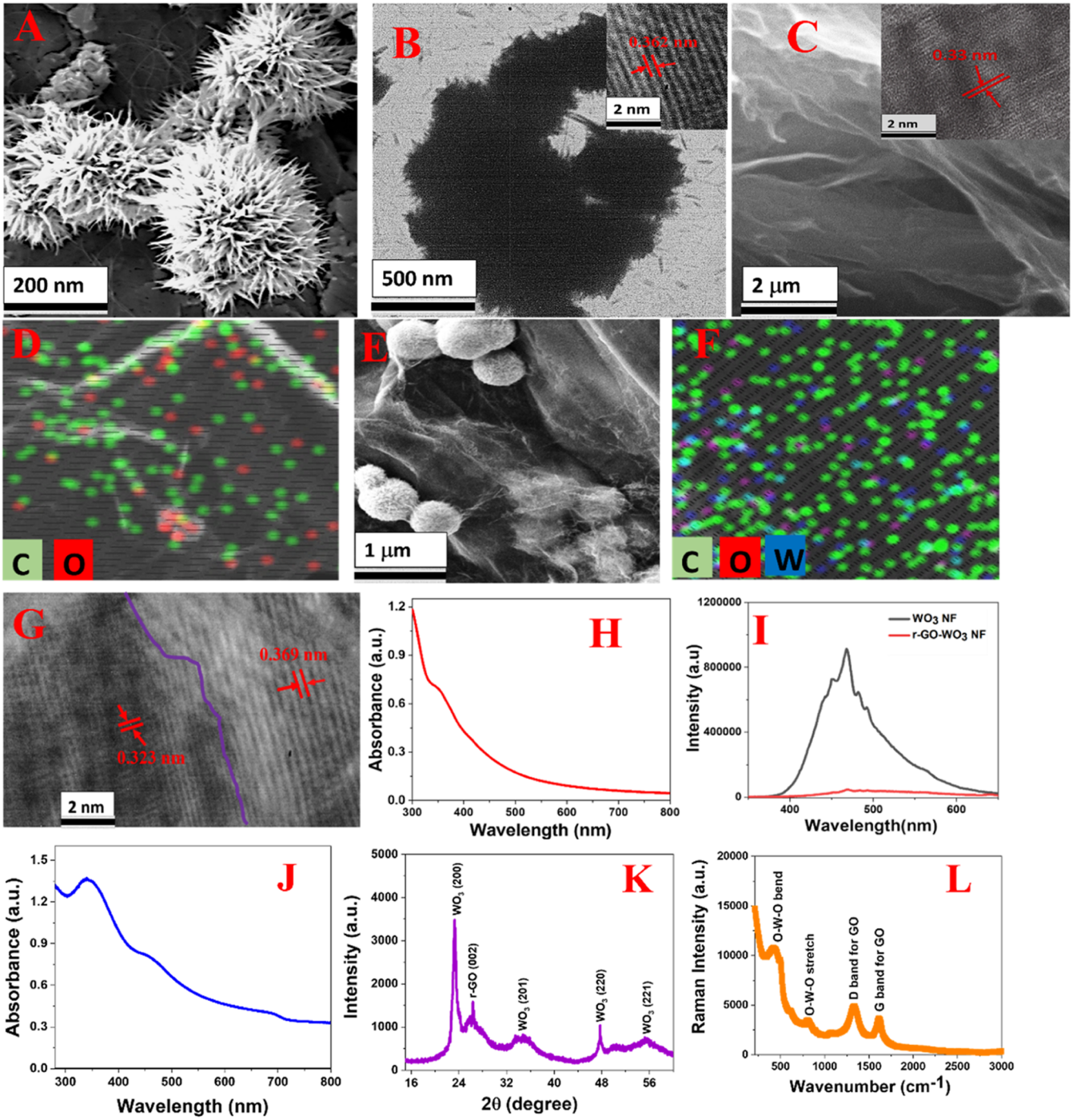

Figure 1. (A) SEM image of the WO_3 nanoflower (WO_3-NF) with a diameter of 200 ± 50 nm. (B) Tunneling electron microscopy (TEM) image of WO_3 NF with a diameter of 200 ± 50 nm. Inset: the HRTEM images show the lattice fringe spacing to be around 0.36 nm, which is due to the (200) crystal plane of monoclinic WO_3. (C) SEM image of reduced graphene oxide (r-GO). Inset: HRTEM images show the lattice fringes spacing to be around 0.34 nm, which is due to the (002) plane of graphene oxide. (D) EDX mapping shows the presence of C and O in reduced graphene oxide. (E) SEM image of WO_3-NF decorated reduced graphene oxide (r-GO) (WO_3 NF/r-GO) heterostructure. (F) EDX mapping shows the presence of W, C, and O in the heterostructure. (G) The HRTEM image from the WO_3 NF/r-GO heterostructure shows different lattice structures around the interface between the WO_3 nanoflower and reduced graphene oxide. (H) Absorption spectra from WO_3 NF. (I) Emission spectra from the WO_3 nanoflower and WO_3 NF/r-GO heterostructure. (J) Absorption spectra from the WO_3 NF/r-GO heterostructure. (K) X-ray diffraction patterns from WO_3 NF/r-GO heterostructure show the (002) planes for r-GO and (200), (201), (220), and (221) planes for monoclinic WO_3. (L) Raman spectra from the WO_3 NF/r-GO heterostructure show the presence of D and G bands from r-GO, the O−W−O stretching and bending band from WO_3-NF, the W−O symmetric stretching from WO_3-NF, and the W−O asymmetric stretching bands from WO_3-NF.

for the freshly prepared WO_3 nanoflower, which indicates that the nanoflower has a diameter of 200 ± 50 nm.[23−26,35−37] The inset HRTEM images in Figure 1B show the lattice fringe spacing to be around 0.36 nm, which is due to the (200) crystal plane of monoclinic WO_3. The X-ray diffraction (XRD) patterns reported in Figure S4 in the Supporting Information

https://doi.org/10.1021/acsomega.5c00054
ACS Omega 2025, 10, 10675−10684

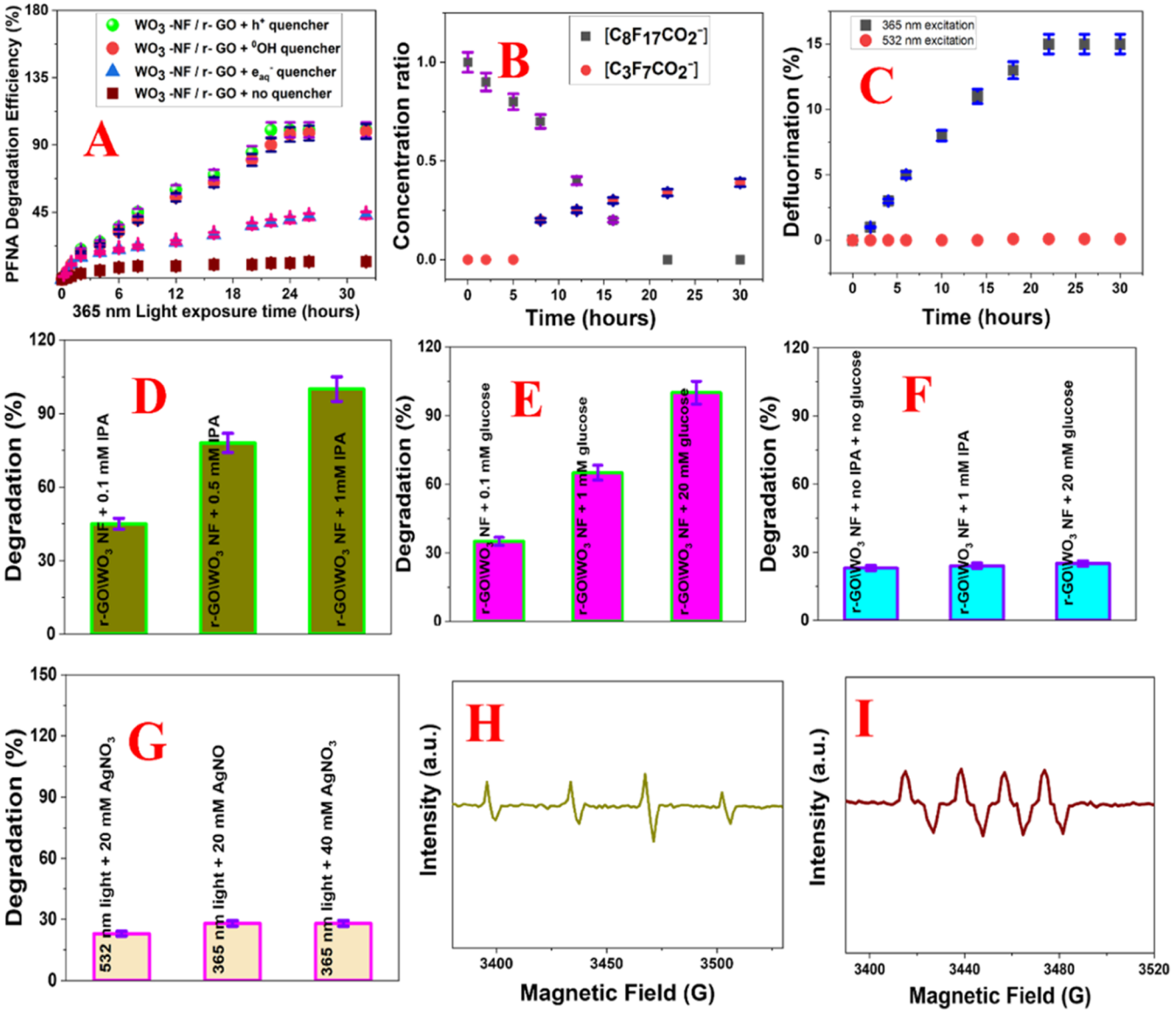

Figure 2. (A) Plot shows how the time-dependent degradation efficiency for PFNA varies in the presence of the WO_3-NF/r-GO binary heterostructure with and without different scavengers after exposure to 365 nm light for different times. Glucose has been used as h^+ quencher, isopropyl alcohol (IPA) has been used as $^{\bullet}OH$ quencher, and silver nitrate has been used as an e_{aq}^- quencher. (B) Plot showing how the concentrations of $C_8F_{17}CO_2^-$ (PFNA anion) and $C_3F_7CO_2^-$ (PFBA anion) vary with time during the degradation of PFNA in the presence of the WO_3-NF/r-GO binary heterostructure and 365 nm light as an excitation source. (C) Plot shows how the defluorination % varies with time during the degradation of PFNA in the presence of the WO_3-NF/r-GO binary heterostructure when they are excited using 365 and 532 nm light as excitation sources separately. (D) Plot shows how the PFNA degradation % varies with hydroxy radical ($^{\bullet}OH$) quencher concentration during the degradation of PFNA in the presence of the WO_3-NF/r-GO binary heterostructure and 365 nm light. (E) Plot shows how the PFNA degradation % varies with hot hole (h^+) quencher concentration during the degradation of PFNA in the presence of the WO_3-NF/r-GO binary heterostructure and 365 nm light. (F) Plot showing how the PFNA degradation % varies with hydroxy radical ($^{\bullet}OH$) quencher and hot hole (h^+) quencher concentrations during the degradation of PFNA in the presence of the WO_3-NF/r-GO binary heterostructure and 532 nm light. (G) Plot shows how the PFNA degradation % varies with hydrated electron (e_{aq}^-) quencher concentration during the degradation of PFNA in the presence of the WO_3-NF/r-GO binary heterostructure and 365/532 nm light excitation separately. (H) Light-irradiated EPR spectra of 5,5-dimethyl-1-pyrroline *N*-oxide (DMPO)-$^{\bullet}OH$ indicating the formation of the hydroxyl radical ($^{\bullet}OH$), during the degradation of PFNA in the presence of the WO_3-NF/r-GO binary heterostructure after exposure of 365 nm light, when silver nitrate was used as an e_{aq}^- quencher. (I) Light-irradiated EPR spectra of DMPO-$^{\bullet}O_2$ indicating the formation of the superoxide anion-free radical ($O_2^{\bullet-}$) during the degradation of PFNA in the presence of the WO_3-NF/r-GO binary heterostructure after exposure to 365 nm light, when glucose was used as an h^+ quencher.

also show the presence of the (200), (201), (220), and (221) planes for monoclinic WO_3 (JCPDS card No. 83-0950).[23−26] Figure S3 in the Supporting Information shows the Raman spectrum of the WO_3 nanoflower, which shows the presence of O−W−O stretching and bending and W−O symmetric stretching bands from WO_3. Figure 1H shows the absorption spectra for WO_3 nanoflower, which indicates strong absorption around 350 nm.

2.3. Synthesis of the WO_3 NF/r-GO Heterostructure. For the development of the WO3 NF/r-GO heterostructure, we have used a surfactant-free solvothermal synthetic approach. Experimental details have been reported in the

https://doi.org/10.1021/acsomega.5c00054
ACS Omega 2025, 10, 10675−10684

Supporting Information. For this purpose, sodium tungsten dehydrate ($Na_2WO_4{\cdot}2H_2O$) was dissolved in 60 mL of deionized water while being stirred at room temperature. After that, it was mixed with 25 mL (1.0 mg/mL) of graphene oxide solution and 0.30 g of oxalic acid ($C_2H_2O_4{\cdot}2H_2O$). In the next step, we have added 60 mL of 100% pure ethanol. Then, the mixture was sonicated for 20 min and transferred into a 100 mL Teflon-lined stainless autoclave. After that, the sample was heated to 200 °C and kept for 24 h at a heating and cooling rate of 5 °C/min. Next, the clear supernatant was collected and separated at 10 000 rpm for 30 min and then washed with distilled water/ethanol (1:1) mixture several times. In the end, the WO_3 NF/r-GO heterostructure was characterized using different spectroscopic and microscopic techniques,[23−26] as reported in the Results and Discussion section.

2.4. Photocatalytic PFNA Degradation Product Analysis. For the analysis of photocatalytic PFNA degradation product, we have used liquid chromatography-mass spectrometry (LC-MS) (Agilent Technologies), as reported by us and others earlier.[10−26] For this purpose, we have used the X Bridge-C18 column (4.6 mm × 250 mm) (Waters Corporation, Milford, MA), proceeded by a C18 guard column (30 × 2.1 mm^2) from the same manufacturer.[23−26] In this case, we used the mobile phase flow at 1 mL/min. For the mass spectrometric analysis, we used negative electrospray ionization and multiple reaction monitoring (MRM) modes.[23−26] Figures S5 and S6 in the Supporting Information show the LC-MS data for PFNA before and after photocatalytic degradation using 355 nm light.

2.5. Measuring Fluoride Ion Concentrations. The amount of fluoride ions (F^-) formed during the photocatalytic degradation was measured using a Dionex-HPIC system (Thermo Fisher Scientific), which is equipped with a conductivity detector.[23−26]

3. RESULTS AND DISCUSSION

3.1. Microscopic and Spectroscopic Characterization of the WO_3 NF/r-GO Heterostructure. Figure 1E shows the SEM image of the WO_3-NF/r-GO binary heterostructure, which indicates that WO_3-NF is decorated on reduced graphene oxide (r-GO). Figure 1F shows the energy-dispersive X-ray (EDX) spectroscopy mapping, which indicates the presence of W, C, and O in the heterostructure. From the above data, we can conclude that the lattice plane structure for WO_3 was slightly affected inside the heterostructure. Figure 1G shows the HRTEM image from the WO_3 NF/r-GO heterostructure, which shows the different lattice structures around the interface (shown in purple line) between the WO_3 nanoflower and reduced graphene oxide. HRTEM images show the lattice fringe spacing to be around 0.37 nm, which is due to the (200) plane of monoclinic WO_3. On the other hand, the inserted HRTEM images from only the WO_3 nanoflower, as reported in Figure 1B, show the lattice fringe spacing to be around 0.36 nm for the (200) plane of monoclinic WO_3. By comparison of the above data, we can conclude that the lattice plane structure for WO_3 was slightly affected inside the heterostructure. Similarly, HRTEM images show the lattice fringe spacing to be around 0.32 nm, which is due to the (002) crystal plane of reduced graphene oxide. However, inserted HRTEM images from only graphene oxide, as reported in Figure 1C, show the lattice fringe spacing to be around 0.33 nm for the (002) plane of graphene oxide. By comparison of the above data, we can conclude that the lattice plane structure for GO was slightly affected by the heterostructure.

Figure 1J shows the absorption spectra from the WO_3 NF/r-GO heterostructure, indicating that λ_{max} is around 365 nm, which is due to the WO_3 NF. The absorption spectra also show the broad absorption band until 800 nm, which is due to r-GO. Similarly, Figure 1I shows the emission spectra from the WO_3 NF/r-GO heterostructure and WO_3 NF separately, which indicates that the emission from WO_3 NF is highly quenched by graphene oxide. Figure 1K shows the X-ray diffraction (XRD) patterns from the WO_3 NF/r-GO heterostructure, which indicates the presence of the (002) planes for r-GO (JCPDS card number 05-0664)[23−26] and the (200), (201), (220), and (221) planes for monoclinic WO_3 (JCPDS Card No. 83-0950).[23−26] Reported XRD data and HRTEM images indicate the presence of monoclinic WO_3 in the heterostructure. Figure 1L shows the Raman spectra from the WO_3 NF/r-GO heterostructure, which indicates the presence of D and G bands from r-GO,[23−26] O−W−O stretching, and bending band from WO_3-NF,[23−26] W−O symmetric stretching from WO_3-NF[23−26], and W−O asymmetric stretching bands from WO_3-NF.[23−26]

3.2. Determining the Perfluorononanoic Acid (PFNA) Degradation Efficiency Using the WO_3-NF/r-GO Binary Heterostructure as a Photocatalyst and 365 nm Light as the Excitation Wavelength. Since the "forever chemicals" like perfluorononanoic acid (PFNA) are difficult to degrade because of their strong carbon−fluorine (C−F) bonds,[10−22] we have performed PFNA degradation experiment using the WO_3-NF/r-GO binary heterostructure at 365 nm light excitation. For the PFNA degradation experiment, we have used 100 μg/L PFNA. As shown Figure 2G, λ_{max} for the WO_3 NF/r-GO heterostructure is around 365 nm, and as a result, we have used a 365 nm diode-pumped solid-state (DPSS) laser with a 150 mW/cm^2 laser power as an excitation light source. To understand the wavelength-dependent PFNA photodegradation experiment, we used a 532 nm visible light also. For this purpose, we used a 532 nm diode-pumped solid-state (DPSS) laser with a 200 mW/cm^2 laser power as the excitation light source.[23−26] The overall defluorination percentage was calculated using eq 1.[5−20]

$$\text{defluorination } \% = \frac{[F^-]}{[C_8F_{17}CO_2H]_0 \times N_{CF}} \times 100 \quad (1)$$

where $[F^-]$ is the measured fluoride ion concentration using a Dionex-HPIC system, $[C_8F_{17}CO_2H]_0$ is the initial PFNA concentration before the degradation experiment, and N_{CF} is the total number of C−F bonds in the PFNA molecule. Using eq 1 and fluoride ion concentration measurement using a Dionex-HPIC system, we determined that the defluorination percentage was ∼14%.

3.3. Understanding the Role of Hydrated Electron, Hot Holes, and ROS for PFNA Degradation Efficiency in the Presence of the WO_3-NF/r-GO Binary Heterostructure after Exposure to 365 nm Light as the Excitation Light Source. As we have discussed before, the photocatalytic efficiency of the WO_3 nanoflower is hindered by the short lifetimes, as well as the mean free path of hot carriers is decreased.[22−36] In the r-GO/WO_3-NF interface, the effective charge transfer from WO_3-NF to r-GO will avoid rapid recombination and improve the probability of hot holes (h^+) and hot electrons participating in PFNA degradation. The possible degradation mechanisms are shown below.

https://doi.org/10.1021/acsomega.5c00054
ACS Omega 2025, 10, 10675−10684

$$WO_3(NF) + h\nu\ (365\ nm) \rightarrow WO_3(NF)[h^+(VB) + e^-(CB)] \quad (2)$$

$$WO_3(e^-) + r\text{-}GO \rightarrow r\text{-}GO(e^-) + WO_3 \quad (3)$$

$$H_2O + r\text{-}GO(e^-) \rightarrow e_{aq}^- + r\text{-}GO \quad (4)$$

$$r\text{-}GO(e^-) + O_2 \rightarrow O_2^{\bullet -} + r\text{-}GO \quad (5)$$

$$h^+ + H_2O \rightarrow {}^{\bullet}OH + H^+ \quad (6)$$

$$PFNA + e_{aq}^- \rightarrow \text{degradation product} \quad (7)$$

$$PFNA + {}^{\bullet}OH \rightarrow \text{degradation product} \quad (8)$$

As shown in eqs 2−8, during photochemical degradation in the presence of the r-GO/WO_3-NF heterostructure and 365 nm excitation light, hydrated electron and different reactive oxygen species such as superoxide anion-free radical ($O_2^{\bullet -}$) and hydroxyl radical ($^{\bullet}OH$) are formed, which plays an important role in the PFNA degradation process. As shown in eq 4, a fraction of the hot electrons interact with water as a solvent and form hydrated electrons (e_{aq}^-),[5−20] which are known to be the most reactive nucleophilic species to cleave C−F bonds.[5−20] Similarly, other hot electrons produce superoxide anion-free radical ($O_2^{\bullet -}$) from O_2, as reported in eq 5. Moreover, as reported in eq 6, hot holes oxidize OH^- or H_2O to produce hydroxy ($^{\bullet}OH$) radicals.

It is now well documented that the quenching effect of hydrated electron (e_{aq}^-) by H^+ can decrease the PFAS degradation efficiency[6−22]; as a result, the reactivity of hydrated electron (e_{aq}^-) is higher under alkaline conditions.[6−22] For this purpose, we performed a photocatalytic degradation experiment at a pH greater than 10. At this pH, the PFNA ($C_8F_{17}CO_2H$) will exist as $C_8F_{17}CO_2^-$. Figure 2A shows that the degradation efficiency is only ∼11% when no scavenger is added. Several recent reports indicate that the quenching effect of the hydrated electron (e_{aq}^-) by the hydroxy radical ($^{\bullet}OH$) can decrease the PFAS degradation efficiency abruptly.[6−22] To avoid the above situation, we have used isopropyl alcohol (IPA) as an $^{\bullet}OH$ quencher.[6−22] As reported in Figure 2A,D, in the presence of IPA as the $^{\bullet}OH$ quencher,[6−22] the PFNA degradation efficiency is enhanced abruptly. The concentration-dependent study reported in Figure 2D indicates that the presence of 1 mM IPA is enough to achieve 100% PFNA degradation. To understand better, we have performed electron paramagnetic resonance (EPR) analysis where we have trapped the hydroxy radical ($^{\bullet}OH$) by using 5,5-dimethyl-1-pyrroline *N*-oxide (DMPO).[6−22] As reported in Figure S7 in the Supporting Information, light-irradiated EPR spectra of DMPO-$^{\bullet}OH$ indicate that the formation of the hydroxyl radical ($^{\bullet}OH$) is not observed during the degradation of PFNA when isopropyl alcohol (IPA) as an $^{\bullet}OH$ quencher is present. On the other hand, as reported in Figure 2H, the formation of the hydroxyl radical ($^{\bullet}OH$) was observed during the degradation of PFNA when IPA as an $^{\bullet}OH$ quencher is absent and silver nitrate as an e_{aq}^- quencher is present.[6−22] By comparing the degradation efficiency in the absence of a quencher, which is only ∼11%, we can conclude that after $^{\bullet}OH$ was quenched by IPA, the hydrated electron utilization efficiency was significantly enhanced.[6−22] As a result, we observed a huge enhancement in the degradation efficiency (∼100%) in the presence of IPA as a $^{\bullet}OH$ quencher.

Moreover, as shown in Figure 2A,E, when glucose was used as a h^+ scavenger,[6−22] 100% degradation was achieved in the presence of the WO_3-NF/r-GO binary heterostructure after exposure to 365 nm light for 22 h. The concentration-dependent study reported in Figure 2E indicates that 20 mM glucose is enough to achieve 100% PFNA degradation. As shown in Figure 1, h^+ oxidizes OH^- or H_2O to produce hydroxy ($^{\bullet}OH$) radicals.[6−22] To understand whether h^+ has been quenched or not in the presence of glucose, we performed the EPR analysis.[6−22] As reported in Figure S8 in the Supporting Information, light-irradiated EPR spectra of DMPO-$^{\bullet}OH$ indicate that the formation of $^{\bullet}OH$ was not observed during the degradation of PFNA when glucose is present as a h^+ quencher. On the other hand, as reported in Figure 2H, light-irradiated EPR spectra indicate the formation of $^{\bullet}OH$ during the degradation of PFNA when glucose is absent as a h^+ quencher, whereas silver nitrate is present as an e_{aq}^- quencher. We have also performed experiments with superoxide dismutase (SOD) as an $O_2^{\bullet -}$ scavenger. We have observed the negligible role of $O_2^{\bullet -}$ in the PFNA degradation process.

Since the hot electron as well as hydrated electron produces superoxide anion-free radical ($O_2^{\bullet -}$) from O_2, we trapped the superoxide radicals $O_2^{\bullet -}$ by using DMPO.[6−22] As reported in Figure 2I, light-irradiated EPR spectra of DMPO-$^{\bullet}O_2$ indicate the formation of the superoxide anion-free radical ($O_2^{\bullet -}$) during the degradation of PFNA when glucose is present as a h^+ quencher. As reported in Figure 2A, the degradation efficiency is only 11% in the absence of any scavenger, which clearly indicates that the h^+ scavenger is crucial for obtaining high PFNA degradation. From all of the quenching experiments ($^{\bullet}OH$ and h^+), we can conclude that the hydrated electron (e_{aq}^-) plays an important role in the significantly enhanced degradation efficiency of PFNA at 365 nm excitation.

Next, to determine the role of a hot hole (h^+) in the degradation of PFNA in the presence of the WO_3-NF/r-GO binary heterostructure and 365 nm light, we used silver nitrate as a quencher for the hydrated electron (e_{aq}^-) and $H^{\bullet}$.[6−22] As shown in Figure 2A,G, when silver nitrate was used as a quencher for the hydrated electron (e_{aq}^-), 28% degradation was achieved in the presence of the WO_3-NF/r-GO binary heterostructure after exposure to 365 nm light for 22 h. Reported experimental data clearly indicate that even without hydrated electron (e_{aq}^-), oxidizing species like hot holes (h^+) and the hydroxyl radical ($^{\bullet}OH$) can also degrade PFNA where the hydroxyl radical ($^{\bullet}OH$) is potentially produced by hot holes (h^+), as reported in Figure 1. The concentration-dependent study, as reported in Figure 2G, indicates that 40 mM silver nitrate is enough to achieve 28% PFNA degradation. To understand this better, we performed electron paramagnetic resonance (EPR) analysis where we trapped the hydroxy radical ($^{\bullet}OH$) by using 5,5-dimethyl-1-pyrroline *N*-oxide (DMPO).[6−22] As reported in Figure 2H, the formation of $^{\bullet}OH$ during the degradation of PFNA is observed when IPA as the $^{\bullet}OH$ quencher is absent and silver nitrate as the e_{aq}^- quencher is present. From all of the quenching study and EPR measurements, we can conclude that synergistic oxidation and reduction are vital for the complete degradation of PFNA, where the hydrated electron (e_{aq}^-) acts as a reducing agent and

https://doi.org/10.1021/acsomega.5c00054
ACS Omega 2025, 10, 10675−10684

hot hole (h^+) and hydroxyl radical ($^{\bullet}OH$) act as oxidation agents.

3.4. Wavelength-Dependent PFNA Degradation Pathways. To understand the PFNA degradation pathway, the degradation products were screened using liquid chromatography-tandem mass spectrometry (LC−MS/MS) techniques, as we have discussed before.[7−27] As reported in Figures 3 and 4, as well as in Tables 1 and 2, two major types

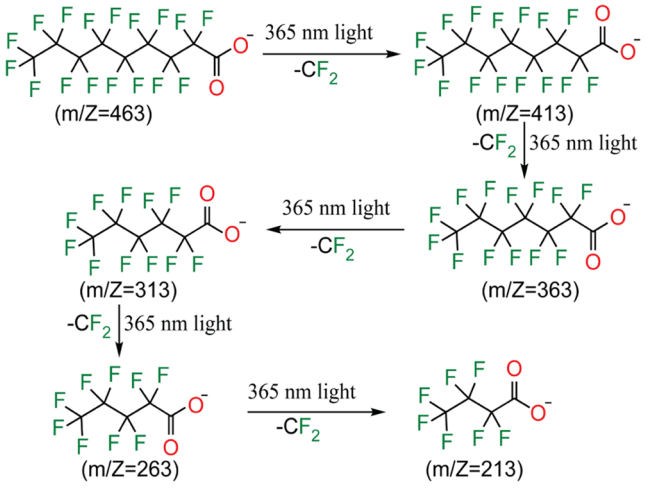

Figure 3. Possible degradation pathways of PFNA via the C−C bond cleavage in the presence of the WO_3-NF/r-GO binary heterostructure and 365 nm light.

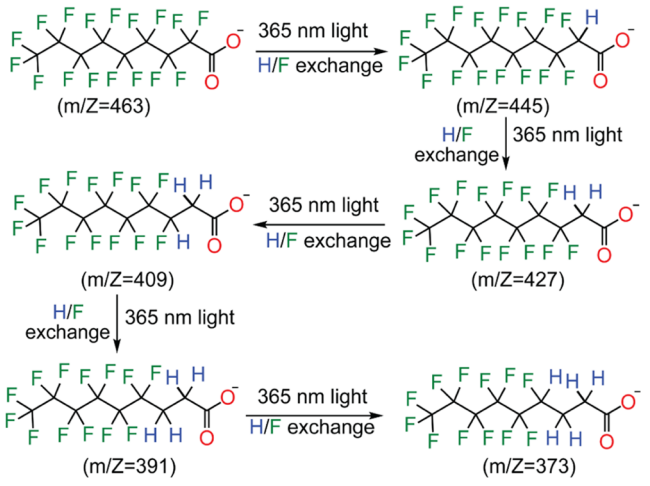

Figure 4. Possible degradation pathways of PFNA via the C−F bond cleavage and H/F exchange in the presence of the WO_3-NF/r-GO binary heterostructure and 365 nm light.

of degradation pathways are observed.[6−22] As reported in Figures 3 and 4, as well as in Table 1, through chain shortening via C−C bond cleavage, a series of shorter-chain PFAS such as $C_7F_{15}CO_2^-$ (m/z = 413), $C_6F_{13}CO_2^-$ (m/z = 363), $C_5F_{11}CO_2^-$ (m/z = 313), $C_4F_9CO_2^-$ (m/z = 263), and $C_3F_7CO_2^-$ (m/z = 213) are produced during the photocatalytic degradation of PFNA. We have not observed any further degradation after $C_3F_7CO_2^-$ (m/z = 213), which is likely due to the higher stability of $C_3F_7CO_2^-$ (m/z = 213) and slower degradation kinetics in the presence of the WO_3-NF/r-GO binary heterostructure under 365 nm light. To understand the chain-shortening pathway, we monitored how the

Table 1. PFNA Photocatalytic Degradation Product Was Observed through Chain Shortening

Product	365 nm excitation	532 nm excitation
 (m/z = 413)	✓	✓
 (m/z = 363)	✓	✓
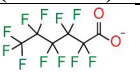 (m/z = 313)	✓	✓
 (m/z = 263)	✓	X
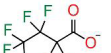 (m/z = 213)	✓	X

Table 2. PFNA photocatalytic degradation product was observed through the C−F bond breaking and H/F exchange

Product	365 nm excitation	532 nm excitation
 (m/z = 445)	✓	X
 (m/z = 427)	✓	X
 (m/z = 409)	✓	X
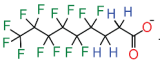 (m/z = 391)	✓	X
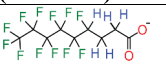 (m/z = 373)	✓	X

concentration of $C_8F_{17}CO_2^-$ (m/z = 463) and $C_3F_7CO_2^-$ (m/z = 213) varies with time during the degradation of PFNA in the presence of the WO_3-NF/r-GO binary heterostructure at 365 nm light excitation. As reported in Figure 2B, we have not observed $C_3F_7CO_2^-$ (m/z = 213) until 5 h of degradation, which is due to the fact that for the formation of $C_3F_7CO_2^-$ (m/z = 213), several C−C band cleavages are necessary as shown in Figure 3. After 5 h of PFNA degradation using the WO_3-NF/r-GO binary heterostructure and 365 nm light, the concentration of $C_3F_7CO_2^-$ (m/z = 213) is enhanced with time.

Similarly, as reported in Figure 4 and Table 2, via C−F bond cleavage and H/F exchange, a series of PFAS products such as $C_8F_{16}HCO_2^-$ (m/z = 445), $C_8F_{15}H_2CO_2^-$ (m/z = 427), $C_8F_{14}H_3CO_2^-$ (m/z = 409), $C_8F_{13}H_4CO_2^-$ (m/z = 391), $C_8F_{12}H_5CO_2^-$ (m/z = 409), $C_7F_{14}HCO_2^-$ (m/z = 395),

https://doi.org/10.1021/acsomega.5c00054
ACS Omega 2025, 10, 10675−10684

$C_7F_{13}H_2CO_2^-$ (m/z = 377), $C_7F_{12}H_3CO_2^-$ (m/z = 359), and $C_7F_{11}H_4CO_2^-$ (m/z = 341) were produced during the photocatalytic degradation of PFNA in the presence of the WO_3-NF/r-GO binary heterostructure at 365 nm light exposure. We did not observe any further H/F exchange after five fluorine atoms for $C_8F_{17}CO_2^-$ (m/z = 463) and four fluorine atoms for $C_7F_{15}CO_2^-$ (m/z = 413), which is mainly due to the slower degradation kinetics in the presence of the WO_3-NF/r-GO binary heterostructure at 365 nm light exposure. We have also not observed any H/F exchange for $C_6F_{13}CO_2^-$ (m/z = 363), $C_5F_{11}CO_2^-$ (m/z = 313), $C_4F_9CO_2^-$ (m/z = 263), and $C_3F_7CO_2^-$ (m/z = 213), which is also due to the slower degradation kinetics in the presence of the WO_3-NF/r-GO binary heterostructure under 365 nm light exposure. To understand the proposed H/F exchange pathway, we have monitored how the concentration of fluoride ion (F^-) varies with time during the degradation of PFNA. As reported in Figure 2C, the plot shows how the defluorination % varies with time during the degradation of PFNA, which clearly indicates that the defluorination % is enhanced with time and reaches the maximum of ∼14% after 22 h.

Next, to understand how the photocatalytic degradation of PFNA varies with excitation wavelength, we performed a PFNA degradation experiment using a WO_3-NF/r-GO binary heterostructure under 532 nm visible light exposure. For the PFNA degradation experiment, we used 100 μg/L PFNA and a 532 nm diode-pumped solid-state (DPSS) laser with 200 mW/cm^2 laser power as the excitation light source. For the analysis of the photocatalytic PFNA degradation product, we used LC-MS (Agilent Technologies) as reported by us and others earlier.[10−27] As reported in Figures 2G and S6 in the Supporting Information, in the presence of silver nitrate (e_{aq}^- quencher), the maximum PFNA degradation efficiency reached ∼22% even after exposure to 532 nm light for 22 h. We also performed the same experiment in the presence of IPA as the $^{\bullet}OH$ quencher or glucose as the h^+ quencher. As reported in Figure S9 in the Supporting Information, the PFNA degradation efficiency was less than 1% even after exposure to 532 nm light for 22 h. The reported experimental data clearly indicates that hydrated electron (e_{aq}^-) is not involved in the PFNA degradation in the presence of the WO_3-NF/r-GO binary heterostructure after exposure to 532 nm light for 22 h. On the other hand, oxidizing species like hot holes (h^+) and the hydroxyl radical ($^{\bullet}OH$) are involved in the degradation of ∼22% PFNA in the presence of the WO_3-NF/r-GO binary heterostructure. As reported in Figure 4 and Table 1, through chain shortening via C−C bond cleavage, a series of shorter-chain PFAS such as $C_7F_{15}CO_2^-$ (m/z = 413), $C_6F_{13}CO_2^-$ (m/z = 363), and $C_5F_{11}CO_2^-$ (m/z = 313) are produced during the photocatalytic degradation of PFNA when exposed to 532 nm light for 22 h. We did not observe any further degradation after $C_5F_{11}CO_2^-$ (m/z = 313), which was likely due to the slower degradation kinetics in the presence of the WO_3-NF/r-GO binary heterostructure at 532 nm light exposure. As reported in Figure 2, the defluorination % is much less than 1% during the photocatalytic degradation of PFNA in the presence of the WO_3-NF/r-GO binary heterostructure at 532 nm light exposure for 22 h. As reported in Figure 4 and Table 2, we have not observed any H/F exchange product during the photocatalytic degradation of PFNA in the presence of the WO_3-NF/r-GO binary heterostructure at 532 nm light exposure for 22 h, which may be due to the lack of the formation of hydrated electrons (e_{aq}^-).

4. CONCLUSIONS

Herein, our findings reveal that 100% PFNA degradation can be achieved in the presence of IPA as $^{\bullet}OH$ quencher or glucose as h^+ quencher when PFNA and r-GO/WO_3 NF heterostructure are exposed to 365 nm light for 22 h. The reported data show two major types of degradation pathways for PFNA degradation in the presence of the r-GO/WO_3 NF heterostructure at 365 nm light exposure. Experimental data shows PFNA degradation via the C−C bond cleavage is a major pathway, whereas PFNA degradation pathway via C−F bond breaking and H/F exchange are the minor pathway. Several experimental data using different scavengers and EPR experiments show that the hydrated electron (e_{aq}^-) plays an important role in obtaining a high degradation efficiency of PFNA at 365 nm excitation. The reported mechanistic study reveals that synergistic oxidation and reduction processes are vital for the complete degradation of PFNA, where the hydrated electron (e_{aq}^-) acts as a reducing agent and hot hole (h^+) and hydroxyl radical ($^{\bullet}OH$) act as oxidation agent. A wavelength-dependent study shows that only 22% degradation can be achieved after exposure to 532 nm light for 24 h, where chain shortening via the C−C bond breaking is the only pathway. The current study shows the significant potential of the photocatalytic r-GO/WO_3 NF heterojunction as a promising platform for the high-efficiency degradation of PFAS at 365 nm excitation.

■ ASSOCIATED CONTENT

Supporting Information

The Supporting Information is available free of charge at https://pubs.acs.org/doi/10.1021/acsomega.5c00054.

Design and characterization of r-GO/WO_3 NF heterostructure catalyst and other experiments such as PFNA degradation (PDF)

■ AUTHOR INFORMATION

Corresponding Author

Paresh Chandra Ray − *Department of Chemistry and Biochemistry, Jackson State University, Jackson, Mississippi 39217, United States;* orcid.org/0000-0001-5398-9930; Email: paresh.c.ray@jsums.edu; Fax: +16019793674

Authors

Kaelin Gates − *Department of Chemistry and Biochemistry, Jackson State University, Jackson, Mississippi 39217, United States*

Shivangee Rai − *Department of Chemistry and Biochemistry, Jackson State University, Jackson, Mississippi 39217, United States*

Avijit Pramanik − *Department of Chemistry and Biochemistry, Jackson State University, Jackson, Mississippi 39217, United States;* orcid.org/0000-0002-4623-2099

Olorunsola Praise Kolawole − *Department of Chemistry and Biochemistry, Jackson State University, Jackson, Mississippi 39217, United States*

Sanchita Kundu − *Department of Chemistry and Biochemistry, Jackson State University, Jackson, Mississippi 39217, United States;* orcid.org/0000-0002-9843-0476

https://doi.org/10.1021/acsomega.5c00054
ACS Omega 2025, 10, 10675−10684

Mine Ucak-Astarlioglu − *US Army Engineer Research and Development Center, Vicksburg, Mississippi 39180-6199, United States;* orcid.org/0000-0003-4186-1707
Manoj K. Shukla − *US Army Engineer Research and Development Center, Vicksburg, Mississippi 39180-6199, United States;* orcid.org/0000-0002-7560-1172
Ahmed Al-Ostaz − *Department of Civil Engineering, University of Mississippi, University, Mississippi 38677, United States*

Complete contact information is available at: https://pubs.acs.org/10.1021/acsomega.5c00054

Notes

The authors declare no competing financial interest.

■ ACKNOWLEDGMENTS

The work described in this document was conducted in the Department of Chemistry at Jackson State University. The authors would like to acknowledge the support provided by the U.S. Army Engineer Research and Development Center (ERDC). The research described and the resulting data presented herein were funded under "Graphene Applications for Military Engineering," under Contract W912HZ-21C0040, managed by the U.S. Army Engineer Research Center. Permission to publish was granted by the ERDC Geotechnical and Structures Laboratory.

■ REFERENCES

(1) United States Environmental Protection Agency. *Drinking Water Health Advisories for PFAS: Fact Sheet for Public Water Systems (PFOA, PFOS, GenX Chemicals and PFBS)*; United States Environmental Protection Agency, 2024. https://www.epa.gov/system/files/documents/2022-06/drinking-water-ha-pfas-factsheet-water-system.pdf (accessed Nov 30, 2024).
(2) *Toxicological Profile for Perfluoroalkyls Atlanta (GA)*; Agency for Toxic Substances and Disease Registry (US), 2021. https://www.atsdr.cdc.gov/toxprofiles/tp200.pdf (accessed Nov 28, 2024).
(3) Zhang, H.; Chen, J.-X.; Qu, J. P.; Kang, Y. B. Photocatalytic low-temperature defluorination of PFASs. *Nature* **2024**, *635*, 210−217.
(4) Evich, M. G.; Davis, M. J. B.; McCord, J. P.; Acrey, B.; Awkerman, J. A.; Knappe, D. R. U.; Lindstrom, A. B.; Speth, T. F.; Tebes-Stevens, C.; Strynar, M. J.; Wang, Z.; Weber, E. J.; Henderson, W. M.; Washington, J. W. Per- and polyfluoroalkyl substances in the environment. *Science* **2022**, *375*, No. eabg9065.
(5) Sonne, C.; Bank, M. S.; Jenssen, B. M.; Cieseielski, T. M.; Rinklebe, J.; Lam, S. S.; Hansen, M.; Bossi, R.; Gustavson, K.; Dietz, R. PFAS pollution threatens ecosystems worldwide. *Science* **2023**, *379*, 887−888.
(6) Trang, B.; Li, Y.; Xue, X.-S.; Atei, M.; Houk, K. N.; Dichtel, W. R. Low-temperature mineralization of perfluorocarboxylic acids. *Science* **2022**, *377*, 839−845.
(7) Wen, Y.; Rentería-Gómez, Á.; Day, G. S.; Smith, M. F.; Yan, T.-H.; Ozdemir, R. O. K.; Gutierrez, O.; Sharma, V. K.; Ma, X.; Zhou, H.-C. Integrated Photocatalytic Reduction and Oxidation of Perfluorooctanoic Acid by Metal−Organic Frameworks: Key Insights into the Degradation Mechanisms. *J. Am. Chem. Soc.* **2022**, *144* (26), 11840−11850.
(8) Guan, Y.; Liu, Z.; Yang, N.; Yang, S.; Quispe-Cardenas, L. E.; Liu, J.; Yang, Y. Near-complete destruction of PFAS in aqueous film-forming foam by integrated photo-electrochemical processes. *Nat. Water* **2024**, *2*, 443−452.
(9) Sinha, S.; Chaturvedi, A.; Gautam, R. K.; Jiang, J. J. Molecular Cu Electrocatalyst Escalates Ambient Perfluorooctanoic Acid Degradation. *J. Am. Chem. Soc.* **2023**, *145*, 27390−27396.
(10) Calvillo Solís, J. J.; Sandoval-Pauker, C.; Bai, D.; Yin, S.; Senftle, T. P.; Villagrán, D. Electrochemical Reduction of Perfluorooctanoic Acid (PFOA): An Experimental and Theoretical Approach. *J. Am. Chem. Soc.* **2024**, *146*, 10687−10698, DOI: 10.1021/jacs.4c00443.
(11) Cui, J.; Gao, P.; Deng, Y. Destruction of Per- and Polyfluoroalkyl Substances (PFAS) with Advanced Reduction Processes (ARPs): A Critical Review. *Environ. Sci. Technol.* **2020**, *54* (7), 3752−3766.
(12) Wang, J.; Lin, Z.; He, X.; Song, M.; Westerhoff, P.; Doudrick, K.; Hanigan, D. Critical Review of Thermal Decomposition of Per- and Polyfluoroalkyl Substances: Mechanisms and Implications for Thermal Treatment Processes. *Environ. Sci. Technol.* **2022**, *56* (9), 5355−5370.
(13) Qi, Y.; Yang, Y.; Cui, S.; Tang, X.; Zhang, P.; Wang, C.; Liang, Y.; Sun, H.; Ma, C.; Xing, B. Novel Defluorination Pathways of Perfluoroether Compounds (GenX): α-Fe2O3 Nanoparticle Layer Retains Higher Concentrations of Effective Hydrated Electrons. *Environ. Sci. Technol.* **2024**, *58* (12), 5567−5577.
(14) Duan, L.; Wang, B.; Heck, K.; Guo, S.; Clark, C. A.; Arredondo, J.; Wang, M.; Senftle, T. P.; Westerhoff, P.; Wen, X.; Song, Y.; Wong, M. S. Efficient Photocatalytic PFOA Degradation over Boron Nitride. *Environ. Sci. Technol. Lett.* **2020**, *7* (8), 613−619.
(15) Liu, X.; Gong, K.; Duan, X.; Wei, W.; Wang, T.; Chen, Z.; Zhang, L.; Ni, B. J. Photo-Induced Bismuth Single Atoms on TiO2 for Highly Efficient Photocatalytic Defluorination of Perfluorooctanoic Acid: Ionization of the C−F Bond. *ACS ES&T Eng.* **2023**, *3* (10), 1626−1636.
(16) Gao, X.; Chen, J.; Che, H.; Ao, Y.; Wang, P. Surface Complex and Nonradical Pathways Contributing to High-Efficiency Degradation of Perfluorooctanoic Acid on Oxygen-Deficient In_2O_3 Derived from an In-Based Metal Organic Framework. *ACS ES&T Water* **2022**, *2* (8), 1344−1352.
(17) Qian, L.; Kopinke, F.-D.; Georgi, A. Photodegradation of Perfluorooctanesulfonic Acid on Fe-Zeolites in Water. *Environ. Sci. Technol.* **2021**, *55* (1), 614−622.
(18) Gu, M.; Li, S.; Fan, X.; Huang, J.; Yu, G. Effective Breaking of the Fluorocarbon Chain by the Interface Bi2O2X···PFOA Complex Strategy via Coordinated Se on Construction of the Internal Photogenerated Carrier Pathway. *ACS Appl. Mater. Interfaces* **2022**, *14* (1), 654−667.
(19) Arima, Y.; Okayasu, Y.; Yoshioka, D.; Nagai, Y.; Kobayashi, Y. Multiphoton-Driven Photocatalytic Defluorination of Persistent Perfluoroalkyl Substances and Polymers by Visible Light. *Angew. Chem., Int. Ed.* **2024**, *63*, No. e202408687, DOI: 10.1002/anie.202408687.
(20) Wang, Z.; Jin, X.; Hong, R.; Wang, X.; Chen, Z.; Gao, G.; He, H.; Liu, J.; Gu, C. New indole derivative heterogeneous system for the synergistic reduction and oxidation of various per-/polyfluoroalkyl substances: insights into the degradation/defluorination mechanism. *Environ. Sci. Technol.* **2023**, *57*, 21459−21469.
(21) Zhang, Y.-J.; Huang, G.-X.; Winter, L. R.; Chen, J.-J.; Tian, L.; Mei, S.-C.; Zhang, Z.; Chen, F.; Guo, Z.-Y.; Ji, R.; You, Y.-Z.; Li, W.-W.; Liu, X.-W.; Yu, H.-Q.; Elimelech, M. Simultaneous nanocatalytic surface activation of pollutants and oxidants for highly efficient water decontamination. *Nat. Commun.* **2022**, *13*, No. 3005.
(22) Liu, G.; Feng, C.; Shao, P. Degradation of Perfluorooctanoic Acid with Hydrated Electron by a Heterogeneous Catalytic System. *Environ. Sci. Technol.* **2022**, *56* (10), 6223−6231.
(23) Pramanik, A.; Kolawole, O. P.; Gates, K.; Kundu, S.; Shukla, M. K.; Moser, R. D.; Ucak-Astarlioglu, M.; Al-Ostaz, A.; Ray, P. C. 2D Fluorinated Graphene Oxide (FGO)-Polyethyleneimine (PEI) Based 3D Porous Nanoplatform for Effective Removal of Forever Toxic Chemicals, Pharmaceutical Toxins, and Waterborne Pathogens from Environmental Water Samples. *ACS Omega* **2023**, *8* (47), 44942−44954.
(24) Pramanik, A.; Kolawole, O. P.; Gates, K.; Kundu, S.; Rai, S.; Shukla, M. K.; Ray, P. C. Cooperative Molecular Interaction-Based Highly Efficient Capturing of Ultrashort- and Short-Chain Emerging Per- and Polyfluoroalkyl Substances Using Multifunctional Nano-adsorbents. *ACS Omega* **2024**, *9* (50), 49452−49462.

(25) Pramanik, A.; Rai, S.; Gates, K.; Kolawole, O. P.; Kundu; Kasani-Akula, P.; Singh, J.; Dasary, J.; Zhang, H.; Han, F. X.; Ray, P. C. Sunlight-Driven Photothermally Boosted Photocatalytic Eradication of Superbugs Using a Plasmonic Gold Nanoparticle-Decorated WO3 Nanowire-Based Heterojunction. *ACS Omega* **2024**, *9* (29), 32256−32267.
(26) Pramanik, A.; Dhar, J. A.; Banerjee, R.; Davis, M.; Gates, K.; Nie, J.; Davis, D.; Han, F. X.; Ray, P. C. WO3 Nanowire-Attached Reduced Graphene Oxide-Based 1D−2D Heterostructures for Near-Infrared Light-Driven Synergistic Photocatalytic and Photothermal Inactivation of Multidrug-Resistant Superbugs. *ACS Appl. Bio Mater.* **2023**, *6* (2), 919−931.
(27) Wei, Z.; Wang, W.; Li, W.; Bai, X.; Zhao, J.; Tse, E. C. M.; Phillips, D. L.; Zhu, Y. Steering Electron-Hole Migration Pathways Using Oxygen Vacancies in Tungsten Oxides to Enhance Their Photocatalytic Oxygen Evolution Performance. *Angew. Chem., Int. Ed.* **2021**, *60* (15), 8236−8242.
(28) Wang, W.; Song, Q.; Luo, Q.; Li, L.; Huo, X.; Chen, S.; Li, J.; Li, Y.; Shi, S.; Yuan, Y.; Du, X.; Zhang, K.; Wang, N. Photothermal-enabled single-atom catalysts for high-efficiency hydrogen peroxide photosynthesis from natural seawater. *Nat. Commun.* **2023**, *14* (1), No. 2493.
(29) Kim, M.; Lee, J. H.; Nam, J. M. Plasmonic Photothermal Nanoparticles for Biomedical Applications. *Adv. Sci.* **2019**, *6* (17), No. 1900471.
(30) Cui, X.; Ruan, Q.; Zhuo, X.; Xia, X.; Hu, J.; Fu, R.; Li, Y.; Wang, J.; Xu, H. Photothermal Nanomaterials: A Powerful Light-to-Heat Converter. *Chem. Rev.* **2023**, *123* (11), 6891−6952.
(31) Yang, B.; Li, C.; Wang, Z.; Dai, Q. Thermoplasmonics in Solar Energy Conversion: Materials, Nanostructured Designs, and Applications. *Adv. Mater.* **2022**, *34*, No. 2107351.
(32) Dooley, M. R.; Nixon, S. P.; Payton, B. E.; Hudak, M. A.; Odei, F.; Vyas, S. Atmospheric Oxidation of PFAS by Hydroxyl Radical: A Density Functional Theory Study. *ACS EST Air* **2024**, *1* (11), 1352−1361.
(33) Paik, T.; Cargnello, M.; Gordon, T. R.; Zhang, S.; Yun, H.; Lee, J. D.; Woo, H. Y.; Oh, S. J.; Kagan, C. R.; Fornasiero, P.; Murray, C. B. Photocatalytic Hydrogen Evolution from Sub stoichiometric Colloidal WO_{3-x} Nanowires. *ACS Energy Lett.* **2018**, *3*, 1904−1910.
(34) Lin, R.; Wan, J.; Xiong, Y.; Wu, K.; Cheong, W.; Zhou, G.; Wang, D.; Peng, Q.; Chen, C.; Li, Y. A. Quantitative Study of Charge Carrier Dynamics in Well-defined WO_3 Nanowires and Nanosheets: Insight into the Crystal Facet Effect in Photocatalysis. *J. Am. Chem. Soc.* **2018**, *140*, 9078−9082.
(35) Sher Shah, M. S. A.; Park, A. R.; Zhang, K.; Park, J. H.; Yoo, P. J. Green synthesis of biphasic TiO_2-reduced graphene oxide nanocomposites with highly enhanced photocatalytic activity. *ACS Appl. Mater. Interfaces* **2012**, *4* (8), 3893−3901.
(36) Negash, A.; Mohammed, S.; Weldekirstos, H. D.; Ambaye, A. D.; Gashu, M. Enhanced photocatalytic degradation of methylene blue dye using eco-friendly synthesized rGO@ZnO nanocomposites. *Sci. Rep.* **2023**, *13* (1), No. 22234.
(37) Kar, S.; Pal, T.; Ghosh, S. Reduced Graphene Oxide−SnSe Nanocomposite Photocatalyst with High Apparent Quantum Yield for the Photodegradation of Norfloxacin. *ACS Appl. Nano Mater.* **2024**, *7* (6), 6516−6524.
(38) Dutta, P.; Karumuthil, S. C.; Roy, R.; Singh, A. K. Highly Stable Poly(o-methoxyaniline)/WO3-Nanoflower Composite-Based Electrochromic Supercapacitors with Real-Time Charge Indication. *ACS Appl. Polym. Mater.* **2023**, *5* (6), 4088−4099.
(39) Bhosale, N. Y.; Mali, S. S.; Hong, C. K.; Kadam, A. V. Hydrothermal synthesis of WO3 nanoflowers on etched ITO and their electrochromic properties. *Electrocchim. Acta* **2017**, *246*, 1112−1120.

https://doi.org/10.1021/acsomega.5c00054
ACS Omega 2025, 10, 10675−10684